ACS APPLIED MATERIALS & INTERFACES

www.acsami.org Research Article

Electroplated Silver−Nickel Core−Shell Nanowire Network Electrodes for Highly Efficient Perovskite Nanoparticle Light-Emitting Diodes

Hyungseok Kang,[#] Seok-Ryul Choi,[#] Young-Hoon Kim, Joo Sung Kim, Sungjin Kim, Byeong-Seon An, Cheol-Woong Yang, Jae-Min Myoung, Tae-Woo Lee, Jung-Gu Kim,* and Jeong Ho Cho*

Cite This: *ACS Appl. Mater. Interfaces* 2020, 12, 39479−39486 Read Online

ABSTRACT: The low sheet resistance and high optical transparency of silver nanowires (AgNWs) make them a promising candidate for use as the flexible transparent electrode of light-emitting diodes (LEDs). In a perovskite LED (PeLED), however, the AgNW electrode can react with the overlying perovskite material by redox reactions, which limit the electroluminescence efficiency of the PeLED by causing the degradation of and generating defect states in the perovskite material. In this study, we prepared Ag−Ni core−shell NW electrodes using the solution-electroplating technique to realize highly efficient PeLEDs based on colloidal formamidinium lead bromide ($FAPbBr_3$) nanoparticles (NPs). Solvated Ni ions from the $NiSO_4$ source were deposited onto the surface of AgNW networks in three steps: (i) cathodic cleaning, (ii) adsorption of the Ni-ion complex onto the AgNW surface, and (iii) uniform electrodeposition of Ni. An ultrathin (∼3.5 nm) Ni layer was uniformly deposited onto the AgNW surface, which exhibited a sheet resistance of 16.7 Ω/sq and an optical transmittance of 90.2%. The Ag−Ni core−shell NWs not only increased the work function of the AgNW electrode, which facilitated hole injection into the emitting layer, but also suppressed the redox reaction between Ag and $FAPbBr_3$ NPs, which prevented the degradation of the emitting layer and the generation of defect states in it. The resulting PeLEDs based on $FAPbBr_3$ NPs with the Ag−Ni core−shell NWs showed high current efficiency of 44.01 cd/A, power efficiency of 35.45 lm/W, and external quantum efficiency of 9.67%.

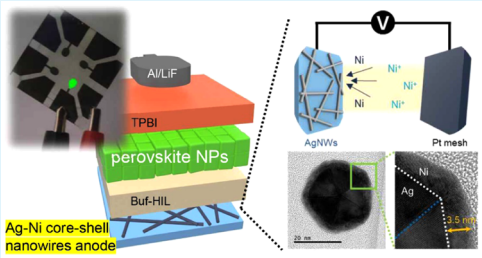

KEYWORDS: *perovskite nanoparticle, electroluminescence efficiency, silver nanowire, electroplating, transparent electrode*

INTRODUCTION

Colloidal metal halide perovskite (ABX_3, where A is an organic ammonium cation (e.g., methylammonium ($CH_3NH_3^+$)), organic ammidinium cation (e.g., formamidinium (FA; $CH(NH_2)_2^+$)), or alkali metal cation (e.g., Cs^+); B is a metal cation (e.g., Pb^{2+}, Sn^{2+}, or Sn^{2+}); and X is a halide anion (I^-, Br^-, or Cl^-)) nanoparticles (NPs) have various advantages, such as narrow emission spectra (full width at half-maximum: 20 nm) with high color purity (color gamut > 95% in the International Telecommunication Union Recommendation BT 2020 standard), high photoluminescence quantum efficiency (PLQE > 90%), easy synthesis, facile color tunability (400 nm ≤ λ ≤ 780 nm), and possible post-treatment.[1−8] Because of these advantages, these materials have been regarded as a suitable choice for emitters in light-emitting diodes (LEDs).[9−13] Recently, the electroluminescence (EL) efficiency of perovskite LEDs (PeLEDs) based on colloidal perovskite NPs[14−17] has been considerably improved via postligand engineering and postanion exchange, and these PeLEDs have been reported to show the highest current efficiency (CE) of 66.7 cd/A and external quantum efficiency (EQE) of 16.48% in green emission[18] and CE of 10.6 cd/A and EQE of 21.3% in red emission.[19] However, these PeLEDs were based on indium tin oxide (ITO) electrodes, which have severe drawbacks such as the following: their price increases frequently because of a scarcity of In sources; they are brittle; they release metallic In and Sn species, which causes quenching of the radiative recombination at the interface between the hole injection layer (HIL) and the emitting layer; they act as trap states, which prevents hole injection into the HIL; and they lower the luminescence efficiency of LEDs.[20,21] Additionally, during the formation of the acidic poly(3,4-ethylenedioxythiophene):polystyrene sulfonate (PEDOT:PSS) HIL, the PSS- groups can adsorb onto the ITO surface, weaken the In−O and Sn−O bonds by protonating ITO, and detach the PSS−In and PSS−Sn complexes from the ITO surface, which can then act as exciton-quenching sites in the emitting layer.[3,22] Therefore,

Received: June 7, 2020
Accepted: July 31, 2020
Published: July 31, 2020

https://dx.doi.org/10.1021/acsami.0c10386
ACS Appl. Mater. Interfaces 2020, 12, 39479−39486

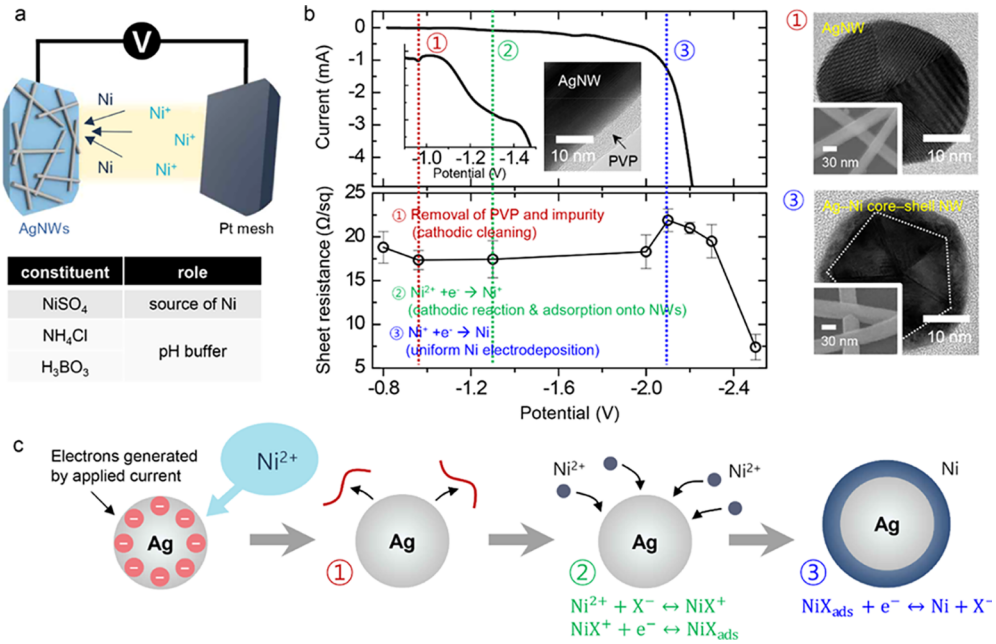

Figure 1. (a) Schematic illustration of the process of Ni electroplating on AgNW network electrode in an electroplating bath. The table lists the constituents of the Ni electroplating bath. (b) LSV sweep results (top panel) and corresponding sheet resistance variation (bottom panel) of AgNW film during Ni electroplating in three steps, as a function of electroplating potential. The sweep rate of the electrode potential during LSV was 20 mV/s. The top-right and bottom-right panels show cross-sectional transmission electron microscopy (TEM) images and top scanning electron microscopy (SEM) images of pristine AgNWs and Ag−Ni core−shell NWs, respectively. (c) Schematic illustration of the process of Ni electroplating on AgNW surface.

alternative ITO-free electrodes that are flexible and chemically inert should be employed in PeLEDs based on colloidal perovskite NPs.

Silver nanowires (AgNWs) are a promising candidate for use as the transparent electrode of flexible LEDs because AgNWs have several advantages, such as a low sheet resistance (<50 Ω/sq), high optical transparency (>90%), and excellent mechanical flexibility.[23−31] The network structure of AgNWs can be easily fabricated through low-cost solution processes (e.g., Meyer-rod coating, spray-coating, and spin-coating).[32−37] In a previous study, these advantages were beneficially utilized to fabricate PeLEDs based on colloidal perovskite NPs on AgNW−polymer composite electrodes. These PeLEDs were fabricated using complex PEDOT:PSS/poly-(*N*-vinyl carbazole) (PVK)/4,4′-cyclohexylidenebis[*N*,*N*-bis(4-methylphenyl)benzeneamine] (TAPC) multilayers, and they showed decent device efficiencies (CE of 10.4 cd/A, power efficiency (PE) of 8.1 lm/W, and EQE of 2.6% for a PeLED based on a AgNW−polymer composite electrode; CE of 9.2 cd/A for a PeLED based on a AgNW−polyimide composite electrode).[38,39] Ag electrodes in these devices can react with perovskite material through redox reactions that convert Pb^{2+} to Pb^0, $MAPbX_3$ to $MA_4PbX_6{\cdot}2H_2O$, and Ag^0 to $Ag^+{-}X^-$,[40] causing degradation of and generating defect states in the perovskite material. If these reactions can be prevented, EL efficiency of PeLEDs can be further improved. Therefore, there is a need to develop metallic electrodes that are chemically stable and do not have any effect on the perovskite material and additionally a HIL that prevents the redox reaction between the electrodes and the perovskite material to increase the EL efficiency of PeLEDs based on colloidal perovskite NPs.

Herein, we report the highly efficient PeLEDs based on colloidal formamidinium ($CH_5N_2^+$; FA^+) lead bromide ($FAPbBr_3$) NPs using electroplated Ag−Ni core−shell NW electrodes and a multifunctional buffer HIL (Buf-HIL). The electroplating of Ni on the AgNWs not only improved their conductivity, because Ni covered both the AgNW surface and the nanogaps among the AgNWs, but also increased the work function of the AgNW electrode, which facilitated hole injection into the emitting layer. Importantly, the Ni shell of the AgNWs suppressed the redox reaction between Ag and the $FAPbBr_3$, which prevented the degradation of the emitting layer and the generation of defect states in it. In addition, the Buf-HIL composed of PEDOT:PSS and perfluorinated ionomer (PFI) further obstructed the reaction between the AgNWs and $FAPbBr_3$ NP films and thus prevented the quenching of the radiative recombination at the HIL−emitting layer interface. Using these strategies, we successfully fabricated efficient PeLEDs with Ag−Ni core−shell NW electrodes having a simplified structure and achieved excellent device performances of the resultant PeLEDs, such as a CE of 44.01 cd/A, PE of 35.45 lm/W, and EQE of 9.67%.

■ RESULTS AND DISCUSSION

Figure 1a shows a schematic illustration of the customized electrochemical deposition process. AgNWs deposited onto a poly(ethylene terephthalate) (PET) substrate (Figures S1 and S2) were used as the cathode electrode, whereas a Pt mesh electrode was utilized as the anode electrode. The Ni electroplating solution was composed of nickel sulfate ($NiSO_4$), ammonium chloride (NH_4Cl), and boric acid (H_3BO_3). $NiSO_4$ was the primary source of Ni ions and was able to deposit Ni onto the AgNW surface.[41,42] The solution pH was carefully considered during selection of the Ni electroplating solution. The thermodynamic stability of the AgNWs, which depends on the solution pH, should be considered to prevent dissolution of the Ag ions present in the AgNWs during exposure to the Ni electroplating solution.

https://dx.doi.org/10.1021/acsami.0c10386
ACS Appl. Mater. Interfaces 2020, 12, 39479−39486

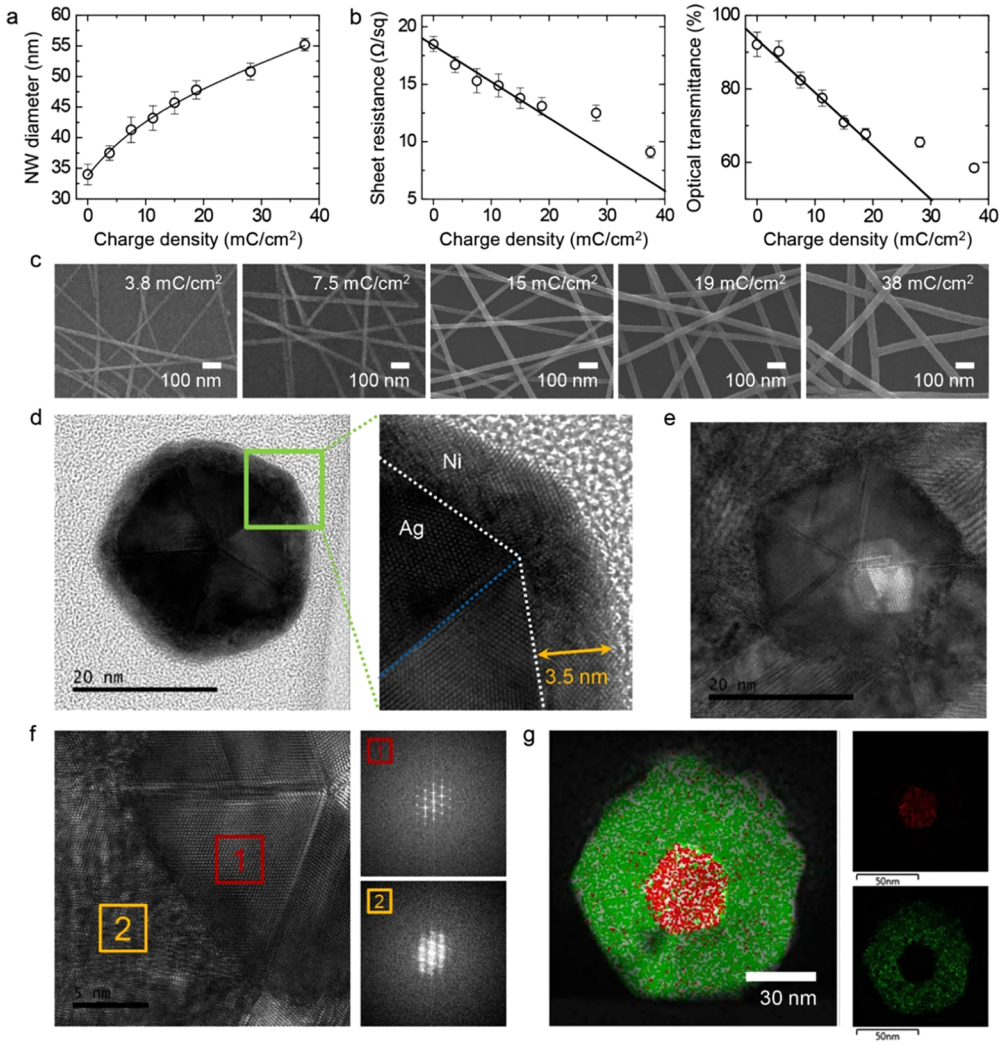

Figure 2. (a) NW diameter and (b) sheet resistance (left) and optical transmittance (right) of Ag−Ni core−shell NW film as functions of charge density. (c) SEM images of Ag−Ni core−shell NW film at various charge densities (3.8, 7.5, 15, 19, and 38 mC/cm^2). (d) Cross-sectional high-resolution TEM (HR-TEM) image of AgNW electroplated with a 3.5 nm thick Ni layer (right panel) and magnified image of Ni-electroplated region (left panel). (e) Cross-sectional HR-TEM image of the thick Ni layer electroplated on AgNW surface at 38 mC/cm^2. (f) FFT analysis results of the cross section of Ag−Ni core−shell NW at two points: (1) AgNW and (2) electroplated Ni. (g) EDS mapping images of the cross section of Ni-electroplated AgNW.

Various Ni electroplating solutions with pH in the range of 3.0−6.2 are available. Because Ag is thermodynamically unstable at pH 5 or lower and likely to exist as Ag^+ ions rather than as a metal in this pH range, it is necessary to adjust the solution pH to the vicinity of 6 to prevent the dissolution of the AgNWs.[43,44]

Both NH_4Cl and H_3BO_3 were selected as pH buffers in this study, and they played a key role in controlling the solution pH. The Ni plating process often involves a side reaction, the hydrogen evolution reaction, which increases the solution pH. The hydrogen evolution reaction consists of two steps.[45] In the first step, hydrogen is adsorbed onto the Ag surface, and the first electron transfer proceeds ($Ag_{(surface)} + H^+ + e^- \leftrightarrow AgH_{(adsorption)}$). In the second step, the second electron transfer proceeds, and electrochemical desorption occurs ($AgH_{(adsorption)} + H^+ + e^- \leftrightarrow Ag_{(surface)} + H_2$). The hydrogen ions in the electrolyte are depleted near the AgNW cathode surface due to the hydrogen evolution reaction. Hence, the pH of the electrolyte near the cathode surface is always maintained at a higher pH than the bulk electrolyte. In this study, to maintain the electroplating bath at pH 6, NH_4Cl and H_3BO_3 were added and the pH was controlled through the following reactions

$$Ni^{2+} + 2H_3BO_3 \leftrightarrow Ni(H_2BO_3)_2 + 2H^+ \quad (1)$$

$$Ni^{2+} + NH_4^+ \leftrightarrow Ni(NH_3)^{2+} + H^+ \quad (2)$$

The distance between the as-coated AgNW electrode and the Pt mesh electrode was maintained constant to apply a uniform current density for the Ni electroplating process. To optimize the electrical conductivity and optical transmittance of the AgNW transparent electrode, Ni plating conditions including the voltage, current density, and electroplating time were systematically controlled.

Linear scan voltammetry (LSV) was employed to study the reduction kinetics of Ni^{2+} from solutions consisting of 150 g/L $NiSO_4$, 15 g/L NH_4Cl, and 15 g/L H_3BO_3 and having pH values in the range of 5.5−6.[46−48] Figure 1b shows the LSV curve and the sheet resistance variation of the AgNWs during the Ni-electrodeposition process as functions of the electro-

https://dx.doi.org/10.1021/acsami.0c10386
ACS Appl. Mater. Interfaces 2020, 12, 39479−39486

plating potential. The Ni electroplating process consisted of three steps, as depicted in Figure 1c: (1) cathodic cleaning, (2) adsorption of the Ni-ion complex onto the AgNWs, and (3) uniform electrodeposition of Ni. In the potential region between −0.8 and −1.8 V versus the Pt electrode, the current remained constant. However, several small current peaks were observed in the magnified plot. A current peak of 0.013 mA was clearly observed at −0.96 V. In this cathodic-cleaning region (step 1), hydrogen was produced on the AgNW surface, and poly(vinyl pyrrolidone) (PVP) or impurities were peeled off from the AgNWs. The transmission electron microscopy (TEM) image in the top-right panel of Figure 1b indicates that no amorphous materials were present on the edge of the AgNWs, which is in strong contrast with the condition of the pristine AgNW (see the TEM image in the inset of the LSV curve in Figure 1b). In the early potential region of the cathodic cleaning, the sheet resistance of the AgNW film decreased slightly from 18.8 to 17 Ω/sq because of the removal of the PVP layer. In step 2 (∼−1.3 V), the Ni^{2+} ions could not be adsorbed directly onto the AgNW surface; therefore, to enable electron transfer, an intermediate step of formation of a cation complex (NiX^+) was required, as given in eq 3, where the anion (X^-) was SO_4^{2-}, OH^-, or Cl^-. At around −1.3 V, a cathodic reaction occurred, but at this stage, Ni was not deposited onto the AgNW surface (Figure S3) despite the increase in the current due to the cathodic reaction. This was because the reaction of the Ni^{2+} ions caused their reduction to Ni^+ ions through the reception of one electron, and a Ni^+-rich region was formed around the AgNW surface (eq 4).

$$Ni^{2+} + X^- \leftrightarrow NiX^+ \quad (3)$$

$$NiX^+ + e^- \leftrightarrow NiX_{ads} \quad (4)$$

$$NiX_{ads} + e^- \leftrightarrow Ni + X^- \quad (5)$$

In the final step, the Ni atoms were deposited onto the AgNW surface at −2 V, according to the reaction expressed in eq 5, and the sheet resistance of the electrode increased from 18.3 to 21.9 Ω/sq. Because of the heterogeneous electroplating of Ni on the AgNW surface, the Ni-electroplated region functioned as a resistor that provided resistance to the flow of electrical current. During electroplating at a potential of −2.1 V or lower, Ni covered the entire AgNW surface, as shown in the TEM and scanning electron microscopy (SEM) images of the Ag−Ni core−shell NWs in the right panel of Figure 1b; from this result, it can be confirmed that Ni was electroplated isotropically on the AgNW surface. In the early potential region, only weak van der Waals interactions occurred between the NWs, which led to interruption of the current flow from NW to NW. However, above the potential of −2.1 V, the diameter of the Ag−Ni core−shell NWs increased and electroplated Ni covered even the nanogaps at the NW junctions, which led to a reduction in the sheet resistance of the AgNW film. On the basis of the LSV sweep results, electroplating was decided to be performed in the galvanostatic mode.

The electrodeposition conditions were optimized by varying the electroplating time at a fixed current density of 1.9 mA/cm^2. Figure 2a shows the variation in the NW diameter with the charge density, which is the current density multiplied by time. As the charge density increased from 0 to 20 mC/cm^2, a fast and linear increase in the NW diameter from 34.0 to 47.8 nm was observed. However, a further increase in the charge density beyond 20 mC/cm^2 resulted in a slower increase in the NW diameter because according to Faraday's law of electrolysis, the cross-sectional area of a NW is proportional to the charge density. At the same time, the sheet resistance of the AgNW film decreased from 18.5 to 9.5 Ω/sq (left graph of Figure 2b) because the NW diameters increased, and the junctions were interlocked. A decrease in the optical transmittance from 92.1 to 58.5% (at 550 nm) was also observed because the electroplated region blocked the open area of the film, as shown in the right panel of Figures 2b and S4. The SEM images of Ni-electroplated AgNWs at various charge densities are shown in Figure 2c (also see atomic force microscopy (AFM) image in Figure S5).

To investigate the crystal growth of Ni on the AgNW surface, the cross-sectional high-resolution TEM (HR-TEM) image of the surface was analyzed. As shown in the left panel of Figure 2d, a thin Ni layer was electrodeposited onto the surface of the core AgNW, which had a completely pentagonal shape and twin boundaries. The magnified image in the right panel of Figure 2d reveals the thickness of the electroplated Ni layer to be approximately 3.5 nm. Atomic reconstruction was observed at the boundary between the electroplated Ni and the AgNW (white dotted line) because of the difference in their lattice parameters. Observation of the thick Ni layer electroplated on the AgNWs in Figures 2e and S6 clearly indicated that this layer had a polycrystalline structure. Ni nucleated in an island form on the AgNW surface at the initial stage of electroplating. The Ni nucleation sites continued to grow laterally along the AgNW surface and formed boundaries when several domains met. Figure 2f shows fast Fourier transform (FFT) analysis results of a cross section of the Ag−Ni core−shell NW. Although the epitaxial crystal structure of the AgNW was clearly observed, the FFT image of the Ni layer in the bottom-right panel of Figure 2f revealed a polycrystalline structure. Energy-dispersive X-ray spectroscopy (EDS) mapping using scanning TEM (STEM) was performed for both the Ag and the Ni elements (Figure 2g). The EDS mapping results showed clear separation between the Ag and Ni signals. The Ag signals (red) were observed only at the center of the NW, but the Ni signals (green) were distributed over the electroplated region (outside the NW). EDS-line-analysis results also demonstrated the successful electroplating of Ni in the shell area (line positions: 0−40 and 70−90 nm) of the Ag core region (line position: 40−70 nm), as shown in Figure S7. Moreover, the junction interlocking by Ni electroplating process notably magnified the mechanical durability of the AgNW network in Figure S8.

AgNWs are susceptible to corrosion, especially in an environment containing moisture, dust, and atmospheric pollutants.[49] Chloride ions (Cl^-) are a significant contaminant in the environment, and their presence can lead to high corrosion rates of Ag. AgCl usually forms on the Ag surface in a physiological NaCl solution.[50] Electrochemical impedance spectroscopy (EIS) was performed to compare the corrosion behaviors of the Ag−Ni core−shell NWs and pristine AgNWs. This corrosion evaluation was performed in an aqueous solution of 3.5 wt % NaCl. Figure 3a shows the EIS diagram in the form of a Nyquist plot. The equivalent circuit shown in Figure 3b was utilized for fitting the EIS data. Here, $R_{solution}$ is the electrolyte resistance, and $R_{charge\ transfer}$ is the charge-transfer resistance at the interface, which is related to the corrosion rate. The constant-phase element (CPE) contains both a double-layer capacitance and a phenomenological coefficient

https://dx.doi.org/10.1021/acsami.0c10386
ACS Appl. Mater. Interfaces 2020, 12, 39479−39486

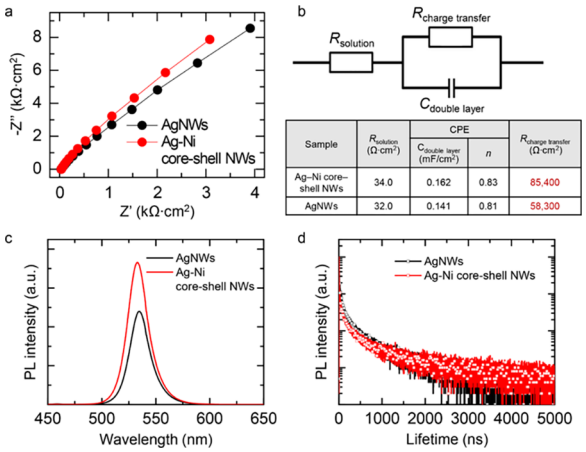

Sample	$R_{solution}$ (Ω·cm²)	CPE		$R_{charge\ transfer}$ (Ω·cm²)
		$C_{double\ layer}$ (mF/cm²)	n	
Ag–Ni core–shell NWs	34.0	0.162	0.83	85,400
AgNWs	32.0	0.141	0.81	58,300

Figure 3. (a) EIS results of pristine AgNWs and Ag−Ni core−shell NWs. (b) EIS equivalent circuit (top) and tabulated EIS fitting data (bottom). (c) PL spectra of perovskite NP films on AgNW/Buf-HIL or Ag−Ni core−shell NW/Buf-HIL structure. (d) PL lifetimes of perovskite NP films on AgNW/Buf-HIL or Ag−Ni core−shell NW/Buf-HIL structure as estimated by TCSPC.

(n), which is described as $Z_{CPE} = 1/[Q(j\omega)^n]$, where Q is a proportionality coefficient, j is an imaginary number, ω is the sine wave modulation angular frequency, and n is an empirical exponent ($0 \leq n \leq 1$) that describes the deviation from the ideal capacitance behavior (i.e., for an ideal capacitor, $n = 1$).[51−54] A high value of $R_{charge\ transfer}$ corresponds to a low corrosion rate. The corresponding fitting results are summarized in the table in Figure 3b. The $R_{charge\ transfer}$ value of the Ag−Ni core−shell NWs was 85 400 Ω·cm², which was higher than that of the pristine AgNWs (58 300 Ω·cm²). This result indicated that the Ag−Ni core−shell NWs showed substantially better corrosion resistance than the pristine AgNWs. Moreover, the Ni shell also improved the stability of the Ag−Ni core−shell NWs at an ambient air temperature of 22 °C and relative humidity (RH) of ∼73% (Figure S9). Stable Ag−Ni core−shell NWs can prevent the diffusion of Ag ions and the redox reaction between Ag ions and perovskite. To evaluate these effects, we fabricated $FAPbBr_3$NP films on a AgNW/Buf-HIL or Ag−Ni core−shell NW/Buf-HIL structure and measured their steady-state photoluminescence (PL) spectra and PL lifetime (Figure 3c,d). The $FAPbBr_3$NP films on the Ag−Ni core−shell NW/Buf-HIL structure showed a higher PL intensity and longer PL lifetime (∼398 ns) than those on the AgNW/Buf-HIL structure (PL lifetime ∼318 ns). These results indicated that the Ni shell suppressed the diffusion of metallic Ag ions, prevented the interaction between the metallic Ag ions and the perovskite NPs, and suppressed the generation of midgap trap state defects, assisting nonradiative recombination of charge carriers in the NP films. The $FAPbBr_3$NP films on the Ag−Ni core−shell NW/Buf-HIL structure also showed a blue-shifted PL peak position (∼533 nm) compared to those on AgNW/Buf-HIL (535 nm), indicating that the Ni shell can suppress the diffusion of defect-inducing Ag ions. This was also confirmed by X-ray photoemission spectroscopy (XPS) analysis of $FAPbBr_3$NP films on AgNWs or Ag−Ni core−shell NW/Buf-HIL structures (Figure S10). Additionally, our Buf-HIL, which consisted of PEDOT:PSS and perfluorinated ionomer (PFI), can prevent the diffusion of Ag ion into the perovskite emitting layer, suppressing the hole trapping in that metal ion.[20,21]

To evaluate our adoption strategies in preventing the generation of metallic Ag ions and for the suppression of their reaction with perovskite NPs, we fabricated PeLEDs based on AgNWs or Ag−Ni core−shell NWs (with a 3.5 nm Ni layer), as shown in Figure 4a (Ag or Ag−Ni core−shell NW/Buf-HIL/$FAPbBr_3$ NP/1,3,5-tris(1-phenyl-1*H*-benzimidazol-2-yl)-benzene (TPBI)/LiF/Al). The electrical and optical parameters were extracted by measuring more than five devices. Note that the Ag−Ni core−shell NWs used for PeLED fabrication exhibited a sheet resistance of 16.7 Ω/sq and an optical transmittance of 90.2%, which was comparable with pristine AgNWs (18.5 Ω/sq and 92.1%) even though 3.5 nm Ni was deposited onto the NW surface (Figure 4b). Figure 4c shows the luminance characteristics of the fabricated PeLEDs. The PeLEDs based on the Ag−Ni core−shell NWs showed lower operating voltages (2.81 V at 1 cd/m², 2.97 V at 10 cd/m², 3.34 V at 100 cd/m², and 4.8 V at 1000 cd/m²) than those based on the pristine AgNWs (2.84 V at 1 cd/m², 3.03 V at 10 cd/m², 3.45 V at 100 cd/m², and n/a at 1000 cd/m²). These results indicated the decreased sheet resistance (16.7 Ω/sq) and increased work function (5.0 eV, Figure S11) of the Ag−Ni core−shell NWs and the suppressed metallic Ag ions, which could act as hole-trapping states in the Buf-HIL-facilitated hole injection into the Buf-HIL and perovskite emitting layer.[38,55] The PeLEDs based on the Ag−Ni core−shell NWs showed higher luminescence efficiencies (CE of 44.01 cd/A, PE of 35.45 lm/W, and EQE of 9.67%) than those based on the

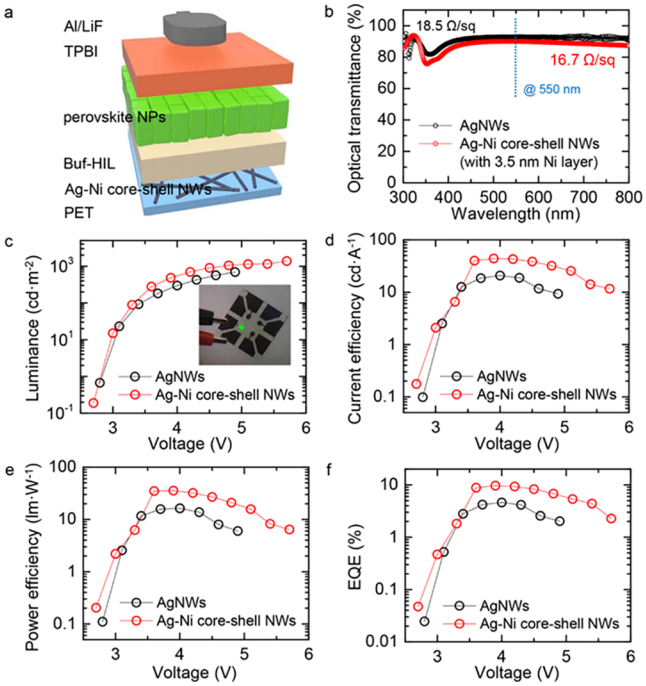

Figure 4. (a) Schematic device structure of PeLED based on Ag−Ni core−shell NW anode. (b) Optical transmittance of pristine AgNWs and Ag−Ni core−shell NWs (with a 3.5 nm Ni layer) as a function of wavelength. (c) Luminance characteristics of PeLEDs based on pristine AgNW and Ag−Ni core−shell NW anodes as functions of applied voltage. The inset shows a photographic image of PeLEDs with Ag−Ni core−shell NWs. (d) CE, (e) PE, and (f) EQE of PeLEDs based on pristine AgNW and Ag−Ni core−shell NW anodes as functions of the applied voltage.

https://dx.doi.org/10.1021/acsami.0c10386
ACS Appl. Mater. Interfaces 2020, 12, 39479−39486

pristine AgNWs (CE of 20.77 cd/A, PE of 16.32 lm/W, and EQE of 4.61%), as shown in Figure 4d–f and Table 1. PeLEDs based on the Ag–Ni core–shell NWs showed bright green emission (inset in Figure 4c) and PeLEDs based on both electrodes showed an EL spectrum with a peak wavelength at 532 nm (Figure S12). These results can be attributed to the following factors: (i) enhanced hole injection into the emitting layer caused by the increased work function and suppressed metallic Ag ions, which can act as hole-trapping states in the Buf-HIL and (ii) suppressed reaction between the metallic Ag ions and the perovskite material and weakened nonradiative recombination of charge carriers in the emitting layer.

Table 1. Luminance Characteristics of AgNWs and Ag–Ni Core–Shell NW-Based PeLEDs

	CE_{max} (cd/A)	PE_{max} (lm/W)	EQE_{max} (%)	L_{max} (cd/m^2)	V_{ON}
AgNWs	20.77	16.32	4.61	693.5	2.804
Ag–Ni core–shell NWs	44.01	35.45	9.67	1378.4	2.716

CONCLUSIONS

We reported the fabrication of highly efficient PeLEDs based on Ag–Ni core–shell NW electrodes. An ultrathin Ni layer was uniformly deposited onto the surface of AgNWs using the electroplating technique. The Ag–Ni core–shell NWs increased the work function of the AgNW electrode, which facilitated hole injection into the perovskite emitting layer. Furthermore, the Ni layer suppressed the redox reaction between Ag and the perovskite material, which prevented the degradation of the emitting layer and the generation of defect states in it. Both these beneficial effects drastically enhanced the electrical performance of the PeLEDs; that is, these devices showed a CE of 44.01 cd/A, PE of 35.45 lm/W, and EQE of 9.67%. The simple and low-cost Ni electroplating technique adopted in this study represents a significant development in the synthesis of flexible and transparent electrodes for next-generation PeLEDs.

ASSOCIATED CONTENT

Supporting Information

The Supporting Information is available free of charge at https://pubs.acs.org/doi/10.1021/acsami.0c10386.

Experimental detail, SEM, TEM, and AFM images of AgNWs; optical transmittance of AgNWs; EDS-line-analysis, XPS, and ultraviolet photoelectron spectroscopy (UPS) results of AgNWs; mechanical and environmental stabilities of AgNWs; electroluminescence spectra of PeLEDs (PDF)

AUTHOR INFORMATION

Corresponding Authors

Jung-Gu Kim – *School of Advanced Materials Science and Engineering, Sungkyunkwan University, Suwon 440-746, Republic of Korea*; Email: kimjg@skku.edu

Jeong Ho Cho – *Department of Chemical and Biomolecular Engineering, Yonsei University, Seoul 03722, Republic of Korea*; orcid.org/0000-0002-1030-9920; Email: jhcho94@yonsei.ac.kr

Authors

Hyungseok Kang – *SKKU Advanced Institute of Nanotechnology (SAINT), Sungkyunkwan University, Suwon 440-746, Republic of Korea*

Seok-Ryul Choi – *School of Advanced Materials Science and Engineering, Sungkyunkwan University, Suwon 440-746, Republic of Korea*

Young-Hoon Kim – *Department of Materials Science and Engineering, School of Chemical and Biological Engineering, Research Institute of Advanced Materials, Institute of Engineering Research, Nano Systems Institute (NSI), BK21 PLUS SNU Materials Division for Educating Creative Global Leaders, Seoul National University, Seoul 08826, Republic of Korea*

Joo Sung Kim – *Department of Materials Science and Engineering, School of Chemical and Biological Engineering, Research Institute of Advanced Materials, Institute of Engineering Research, Nano Systems Institute (NSI), BK21 PLUS SNU Materials Division for Educating Creative Global Leaders, Seoul National University, Seoul 08826, Republic of Korea*

Sungjin Kim – *Department of Materials Science and Engineering, School of Chemical and Biological Engineering, Research Institute of Advanced Materials, Institute of Engineering Research, Nano Systems Institute (NSI), BK21 PLUS SNU Materials Division for Educating Creative Global Leaders, Seoul National University, Seoul 08826, Republic of Korea*

Byeong-Seon An – *School of Advanced Materials Science and Engineering, Sungkyunkwan University, Suwon 440-746, Republic of Korea*; orcid.org/0000-0002-3994-555X

Cheol-Woong Yang – *School of Advanced Materials Science and Engineering, Sungkyunkwan University, Suwon 440-746, Republic of Korea*; orcid.org/0000-0003-0475-8399

Jae-Min Myoung – *Department of Materials Science and Engineering, Yonsei University, Seoul 03722, Republic of Korea*; orcid.org/0000-0003-4724-0653

Tae-Woo Lee – *Department of Materials Science and Engineering, School of Chemical and Biological Engineering, Research Institute of Advanced Materials, Institute of Engineering Research, Nano Systems Institute (NSI), BK21 PLUS SNU Materials Division for Educating Creative Global Leaders, Seoul National University, Seoul 08826, Republic of Korea*; orcid.org/0000-0002-6449-6725

Complete contact information is available at: https://pubs.acs.org/10.1021/acsami.0c10386

Author Contributions

#H.K. and S.-R.C. contributed equally to this work.

Notes

The authors declare no competing financial interest.

ACKNOWLEDGMENTS

This work was supported by the Samsung Research Funding & Incubation Center of Samsung Electronics under Project Number SRFC-MA1901-01.

REFERENCES

(1) Ha, S.-T.; Su, R.; Xing, J.; Zhang, Q.; Xiong, Q. Metal Halide Perovskite Nanomaterials: Synthesis and Applications. *Chem. Sci.* **2017**, *8*, 2522–2536.

(2) Huang, H.; Bodnarchuk, M. I.; Kershaw, S. V.; Kovalenko, M. V.; Rogach, A. L. Lead Halide Perovskite Nanocrystals in the Research

Spotlight: Stability and Defect Tolerance. *ACS Energy Lett.* **2017**, *2*, 2071−2083.
(3) Kim, Y. H.; Kim, J. S.; Lee, T. W. Strategies to Improve Luminescence Efficiency of Metal-Halide Perovskites and Light-Emitting Diodes. *Adv. Mater.* **2019**, *31*, No. 1804595.
(4) Kim, Y.-H.; Cho, H.; Lee, T.-W. Metal Halide Perovskite Light Emitters. *Proc. Natl. Acad. Sci. U.S.A.* **2016**, *113*, 11694−11702.
(5) Kim, Y.-H.; Lee, G.-H.; Kim, Y.-T.; Wolf, C.; Yun, H. J.; Kwon, W.; Park, C. G.; Lee, T.-W. High Efficiency Perovskite Light-Emitting Diodes of Ligand-Engineered Colloidal Formamidinium Lead Bromide Nanoparticles. *Nano Energy* **2017**, *38*, 51−58.
(6) Kim, Y.-H.; Wolf, C.; Kim, Y.-T.; Cho, H.; Kwon, W.; Do, S.; Sadhanala, A.; Park, C. G.; Rhee, S.-W.; Im, S. H.; et al. Highly Efficient Light-Emitting Diodes of Colloidal Metal−Halide Perovskite Nanocrystals Beyond Quantum Size. *ACS Nano* **2017**, *11*, 6586−6593.
(7) Protesescu, L.; Yakunin, S.; Bodnarchuk, M. I.; Krieg, F.; Caputo, R.; Hendon, C. H.; Yang, R. X.; Walsh, A.; Kovalenko, M. Nanocrystals of Cesium Lead Halide Perovskites (CsPbX3, X= Cl, Br, and I): Novel Optoelectronic Materials Showing Bright Emission with Wide Color Gamut. *Nano Lett.* **2015**, *15*, 3692−3696.
(8) Veldhuis, S. A.; Boix, P. P.; Yantara, N.; Li, M.; Sum, T. C.; Mathews, N.; Mhaisalkar, S. G. Perovskite Materials for Light-Emitting Diodes and Lasers. *Adv. Mater.* **2016**, *28*, 6804−6834.
(9) Hou, J.; Yin, X.; Fang, Y.; Huang, F.; Jiang, W. Novel Red-Emitting Perovskite-Type Phosphor Cala1− Xmgm′ O6: Xeu3+ (M′= Nb, Ta) for White Led Application. *Opt. Mater.* **2012**, *34*, 1394−1397.
(10) Lin, K.; Xing, J.; Quan, L. N.; de Arquer, F. P. G.; Gong, X.; Lu, J.; Xie, L.; Zhao, W.; Zhang, D.; Yan, C.; et al. Perovskite Light-Emitting Diodes with External Quantum Efficiency Exceeding 20 Per Cent. *Nature* **2018**, *562*, 245−248.
(11) Wang, N.; Cheng, L.; Ge, R.; Zhang, S.; Miao, Y.; Zou, W.; Yi, C.; Sun, Y.; Cao, Y.; Yang, R.; et al. Perovskite Light-Emitting Diodes Based on Solution-Processed Self-Organized Multiple Quantum Wells. *Nat. Photonics* **2016**, *10*, 699−704.
(12) Yuan, M.; Quan, L. N.; Comin, R.; Walters, G.; Sabatini, R.; Voznyy, O.; Hoogland, S.; Zhao, Y.; Beauregard, E. M.; Kanjanaboos, P.; et al. Perovskite Energy Funnels for Efficient Light-Emitting Diodes. *Nat. Nanotechnol.* **2016**, *11*, 872−877.
(13) Zhang, L.; Yang, X.; Jiang, Q.; Wang, P.; Yin, Z.; Zhang, X.; Tan, H.; Yang, Y. M.; Wei, M.; Sutherland, B. R. Ultra-Bright and Highly Efficient Inorganic Based Perovskite Light-Emitting Diodes. *Nat. Commun.* **2017**, *8*, No. 15640.
(14) Shan, Q.; Song, J.; Zou, Y.; Li, J.; Xu, L.; Xue, J.; Dong, Y.; Han, B.; Chen, J.; Zeng, H. High Performance Metal Halide Perovskite Light-Emitting Diode: From Material Design to Device Optimization. *Small* **2017**, *13*, No. 1701770.
(15) Wei, Z.; Perumal, A.; Su, R.; Sushant, S.; Xing, J.; Zhang, Q.; Tan, S. T.; Demir, H. V.; Xiong, Q. Solution-Processed Highly Bright and Durable Cesium Lead Halide Perovskite Light-Emitting Diodes. *Nanoscale* **2016**, *8*, 18021−18026.
(16) Xing, J.; Yan, F.; Zhao, Y.; Chen, S.; Yu, H.; Zhang, Q.; Zeng, R.; Demir, H. V.; Sun, X.; Huan, A.; et al. High-Efficiency Light-Emitting Diodes of Organometal Halide Perovskite Amorphous Nanoparticles. *ACS Nano* **2016**, *10*, 6623−6630.
(17) Zhang, X.; Xu, B.; Zhang, J.; Gao, Y.; Zheng, Y.; Wang, K.; Sun, X. W. All-Inorganic Perovskite Nanocrystals for High-Efficiency Light Emitting Diodes: Dual-Phase CsPbBr3-CsPb2Br5 Composites. *Adv. Funct. Mater.* **2016**, *26*, 4595−4600.
(18) Song, J.; Fang, T.; Li, J.; Xu, L.; Zhang, F.; Han, B.; Shan, Q.; Zeng, H. Organic−Inorganic Hybrid Passivation Enables Perovskite Qleds with an Eqe of 16.48%. *Adv. Mater.* **2018**, *30*, No. 1805409.
(19) Chiba, T.; Hayashi, Y.; Ebe, H.; Hoshi, K.; Sato, J.; Sato, S.; Pu, Y.-J.; Ohisa, S.; Kido, J. Anion-Exchange Red Perovskite Quantum Dots with Ammonium Iodine Salts for Highly Efficient Light-Emitting Devices. *Nat. Photonics* **2018**, *12*, 681−687.
(20) Seo, H. K.; Kim, H.; Lee, J.; Park, M. H.; Jeong, S. H.; Kim, Y. H.; Kwon, S. J.; Han, T. H.; Yoo, S.; Lee, T. W. Efficient Flexible Organic/Inorganic Hybrid Perovskite Light-Emitting Diodes Based on Graphene Anode. *Adv. Mater.* **2017**, *29*, No. 1605587.
(21) Han, T.-H.; Lee, Y.; Choi, M.-R.; Woo, S.-H.; Bae, S.-H.; Hong, B. H.; Ahn, J.-H.; Lee, T.-W. Extremely Efficient Flexible Organic Light-Emitting Diodes with Modified Graphene Anode. *Nat. Photonics* **2012**, *6*, 105−110.
(22) Mammana, S. S.; Greatti, A.; Luiz, F. H.; da Costa, F. I.; Mammana, A. P.; Calligaris, G. A.; Cardoso, L. P.; Mammana, C. I. Z.; den Engelsen, D. Study of Wet Etching Thin Films of Indium Tin Oxide in Oxalic Acid by Monitoring the Resistance. *Thin Solid Films* **2014**, *567*, 20−31.
(23) An, B. W.; Hyun, B. G.; Kim, S.-Y.; Kim, M.; Lee, M.-S.; Lee, K.; Koo, J. B.; Chu, H. Y.; Bae, B.-S.; Park, J.-U. Stretchable and Transparent Electrodes Using Hybrid Structures of Graphene−Metal Nanotrough Networks with High Performances and Ultimate Uniformity. *Nano Lett.* **2014**, *14*, 6322−6328.
(24) De, S.; Higgins, T. M.; Lyons, P. E.; Doherty, E. M.; Nirmalraj, P. N.; Blau, W. J.; Boland, J. J.; Coleman, J. N. Silver Nanowire Networks as Flexible, Transparent, Conducting Films: Extremely High DC to Optical Conductivity Ratios. *ACS Nano* **2009**, *3*, 1767−1774.
(25) Kang, H.; Song, S.-J.; Sul, Y. E.; An, B.-S.; Yin, Z.; Choi, Y.; Pu, L.; Yang, C.-W.; Kim, Y. S.; Cho, S. M. Epitaxial-Growth-Induced Junction Welding of Silver Nanowire Network Electrodes. *ACS Nano* **2018**, *12*, 4894−4902.
(26) Kang, H.; Yi, G.-R.; Kim, Y. J.; Cho, J. H. Junction Welding Techniques for Metal Nanowire Network Electrodes. *Macromol. Res.* **2018**, *26*, 1066−1073.
(27) Kang, H.; Zhao, C.; Huang, J.; Ho, D. H.; Megra, Y. T.; Suk, J. W.; Sun, J.; Wang, Z. L.; Sun, Q.; Cho, J. H. Fingerprint-Inspired Conducting Hierarchical Wrinkles for Energy-Harvesting E-Skin. *Adv. Funct. Mater.* **2019**, *29*, No. 1903580.
(28) Madaria, A. R.; Kumar, A.; Ishikawa, F. N.; Zhou, C. Uniform, Highly Conductive, and Patterned Transparent Films of a Percolating Silver Nanowire Network on Rigid and Flexible Substrates Using a Dry Transfer Technique. *Nano Res.* **2010**, *3*, 564−573.
(29) Park, J. H.; Hwang, G. T.; Kim, S.; Seo, J.; Park, H. J.; Yu, K.; Kim, T. S.; Lee, K. J. Flash-Induced Self-Limited Plasmonic Welding of Silver Nanowire Network for Transparent Flexible Energy Harvester. *Adv. Mater.* **2017**, *29*, No. 1603473.
(30) Shiau, Y.-J.; Chiang, K.-M.; Lin, H.-W. Performance Enhancement of Metal Nanowire-Based Transparent Electrodes by Electrically Driven Nanoscale Nucleation of Metal Oxides. *Nanoscale* **2015**, *7*, 12698−12705.
(31) Chang, J.-H.; Chiang, K.-M.; Kang, H.-W.; Chi, W.-J.; Chang, J.-H.; Wu, C.-I.; Lin, H.-W. A Solution-Processed Molybdenum Oxide Treated Silver Nanowire Network: A Highly Conductive Transparent Conducting Electrode with Superior Mechanical and Hole Injection Properties. *Nanoscale* **2015**, *7*, 4572−4579.
(32) Cheong, H.-G.; Triambulo, R. E.; Lee, G.-H.; Yi, I.-S.; Park, J.-W. Silver Nanowire Network Transparent Electrodes with Highly Enhanced Flexibility by Welding for Application in Flexible Organic Light-Emitting Diodes. *ACS Appl. Mater. Interfaces* **2014**, *6*, 7846−7855.
(33) Kim, T.; Canlier, A.; Kim, G. H.; Choi, J.; Park, M.; Han, S. M. J. A. a. m. Electrostatic Spray Deposition of Highly Transparent Silver Nanowire Electrode on Flexible Substrate. *ACS Appl. Mater. Interfaces* **2013**, *5*, 788−794.
(34) Lee, H.; Lee, D.; Ahn, Y.; Lee, E.-W.; Park, L. S.; Lee, Y. Highly Efficient and Low Voltage Silver Nanowire-Based Oleds Employing a N-Type Hole Injection Layer. *Nanoscale* **2014**, *6*, 8565−8570.
(35) Lee, S. J.; Kim, Y.-H.; Kim, J. K.; Baik, H.; Park, J. H.; Lee, J.; Nam, J.; Park, J. H.; Lee, T.-W.; Yi, G.-R. A Roll-to-Roll Welding Process for Planarized Silver Nanowire Electrodes. *Nanoscale* **2014**, *6*, 11828−11834.
(36) Liu, Y.-s.; Feng, J.; Ou, X.-L.; Cui, H.-f.; Xu, M.; Sun, H.-B. Ultrasmooth, Highly Conductive and Transparent Pedot: Pss/Silver Nanowire Composite Electrode for Flexible Organic Light-Emitting Devices. *Org. Electron.* **2016**, *31*, 247−252.

https://dx.doi.org/10.1021/acsami.0c10386
ACS Appl. Mater. Interfaces 2020, 12, 39479−39486

(37) Scardaci, V.; Coull, R.; Lyons, P. E.; Rickard, D.; Coleman, J. N. Spray Deposition of Highly Transparent, Low-Resistance Networks of Silver Nanowires over Large Areas. *Small* **2011**, *7*, 2621−2628.
(38) Li, Y. F.; Chou, S. Y.; Huang, P.; Xiao, C.; Liu, X.; Xie, Y.; Zhao, F.; Huang, Y.; Feng, J.; Zhong, H. Stretchable Organometal-Halide-Perovskite Quantum-Dot Light-Emitting Diodes. *Adv. Mater.* **2019**, *31*, No. 1807516.
(39) Zhao, F.; Chen, D.; Chang, S.; Huang, H.; Tong, K.; Xiao, C.; Chou, S.; Zhong, H.; Pei, Q. Highly Flexible Organometal Halide Perovskite Quantum Dot Based Light-Emitting Diodes on a Silver Nanowire−Polymer Composite Electrode. *J. Mater. Chem. C* **2017**, *5*, 531−538.
(40) Kato, Y.; Ono, L. K.; Lee, M. V.; Wang, S.; Raga, S. R.; Qi, Y. Silver Iodide Formation in Methyl Ammonium Lead Iodide Perovskite Solar Cells with Silver Top Electrodes. *Adv. Mater. Interfaces* **2015**, *2*, No. 1500195.
(41) Grujicic, D.; Pesic, B. Electrochemical and Afm Study of Nickel Nucleation Mechanisms on Vitreous Carbon from Ammonium Sulfate Solutions. *Electrochim. Acta* **2006**, *51*, 2678−2690.
(42) Ji, J.; Cooper, W.; Dreisinger, D.; Peters, E. Surface Ph Measurements During Nickel Electrodeposition. *J. Appl. Electrochem.* **1995**, *25*, 642−650.
(43) Elechiguerra, J. L.; Larios-Lopez, L.; Liu, C.; Garcia-Gutierrez, D.; Camacho-Bragado, A.; Yacaman, M. J. Corrosion at the Nanoscale: The Case of Silver Nanowires and Nanoparticles. *Chem. Mater.* **2005**, *17*, 6042−6052.
(44) Delahay, P.; Pourbaix, M.; Van Rysselberghe, P. Potential-Ph Diagram of Silver Construction of the Diagram—Its Applications to the Study of the Properties of the Metal, Its Compounds, and Its Corrosion. *J. Electrochem. Soc.* **1951**, *98*, 65−67.
(45) Šupicová, M.; Rozik, R.; Trnkova, L.; Oriňáková, R.; Galova, M. Influence of Boric Acid on the Electrochemical Deposition of Ni. *J. Solid State Electrochem.* **2006**, *10*, 61−68.
(46) Low, C.; Walsh, F. Linear Sweep Voltammetry of the Electrodeposition of Copper from a Methanesulfonic Acid Bath Containing a Perfluorinated Cationic Surfactant. *Surf. Coat. Technol.* **2008**, *202*, 3050−3057.
(47) Oriňáková, R.; Strečková, M.; Trnkova, L.; Rozik, R.; Galova, M. Comparison of Chloride and Sulphate Electrolytes in Nickel Electrodeposition on a Paraffin Impregnated Graphite Electrode. *J. Electroanal. Chem.* **2006**, *594*, 152−159.
(48) López, J. R.; Méndez, P.; Bueno, J. P.; Trejo, G.; Antaño, R.; Torres-González, J.; Stremsdoerfer, G.; Meas, Y. Samarium Additive Effect onto the Nickel Electrodeposition Process. *J. Electrochem. Soc.* **2017**, *164*, D524−D531.
(49) Graedel, T. E. Corrosion Mechanisms for Silver Exposed to the Atmosphere. *J. Electrochem. Soc.* **1992**, *139*, 1963−1970.
(50) Ha, H.; Payer, J. The Effect of Silver Chloride Formation on the Kinetics of Silver Dissolution in Chloride Solution. *Electrochim. Acta* **2011**, *56*, 2781−2791.
(51) Chassaing, E.; Joussellin, M.; Wiart, R. The Kinetics of Nickel Electrodeposition: Inhibition by Adsorbed Hydrogen and Anions. *J. Electroanal. Chem.* **1983**, *157*, 75−88.
(52) Hamdy, A. S.; El-Shenawy, E.; El-Bitar, T. Electrochemical Impedance Spectroscopy Study of the Corrosion Behavior of Some Niobium Bearing Stainless Steels in 3.5% Nacl. *Int. J. Electrochem. Sci.* **2006**, *1*, 171−180.
(53) Zhang, P.; Wu, J.; Zhang, W.; Lu, X.; Wang, K. A Pitting Mechanism for Passive 304 Stainless Steel in Sulphuric Acid Media Containing Chloride Ions. *Corros. Sci.* **1993**, *34*, 1343−1354.
(54) Park, I.-J.; Choi, S.-R.; Kim, J.-G. Aluminum Anode for Aluminum-Air Battery−Part Ii: Influence of in Addition on the Electrochemical Characteristics of Al-Zn Alloy in Alkaline Solution. *J. Power Sources* **2017**, *357*, 47−55.
(55) Eom, H.; Lee, J.; Pichitpajongkit, A.; Amjadi, M.; Jeong, J. H.; Lee, E.; Lee, J. Y.; Park, I. Ag@ Ni Core−Shell Nanowire Network for Robust Transparent Electrodes against Oxidation and Sulfurization. *Small* **2014**, *10*, 4171−4181.

https://dx.doi.org/10.1021/acsami.0c10386
ACS Appl. Mater. Interfaces 2020, 12, 39479−39486